

## MEASUREMENTS OF PRESSURE DISTRIBUTION BY INTEGRATING THE MATERIAL ACCELERATION

Xiaofeng Liu and Joseph Katz  
Department of Mechanical Engineering  
Whiting School of Engineering  
Johns Hopkins University  
Baltimore, Maryland 21218  
USA  
xliu2001@jhu.edu  
katz@titan.me.jhu.edu

## ABSTRACT

This paper describes the development of a measurement system that is capable of measuring the instantaneous pressure distribution over a sample area in a turbulent flow field. The technique utilizes four-exposure PIV to measure the material acceleration of the flow and integrating it to obtain the pressure distribution. If necessary, e.g., for cavitation test, a reference pressure at a single reference point is also required. Two 2K×2K CCD cameras and perpendicularly polarized Nd:Yag lasers are used for recording four exposures, with images one and three recorded by camera one to provide the first velocity vector map, and images two and four recorded by camera two to provide the second velocity vector map. The material acceleration is calculated from the velocity difference in sample areas that are shifted relative to each other according to the local velocity. Averaged omni-directional integration of the material acceleration, avoiding regions dominated by viscous diffusion, provides the pressure distribution. To improve the accuracy of the acceleration measurement, cross-correlation of the corresponding image correlation maps is implemented at areas with high velocity gradient. Applications of these procedures to synthetic images of rotational and stagnation point flows show that the relative error of the measured pressure is 4.0% at the 95% confidence level. The system is presently being used to measure the instantaneous pressure and velocity distributions of a 2D cavity flow field in a water tunnel.

## NOMENCLATURE

$C_p$  pressure coefficient,  $C_p = (p - p_{ref}) / (0.5 \rho U_e^2)$   
 $\frac{D\bar{U}}{Dt}$  material (Lagrangian) acceleration  
 $p$  pressure  
 $p_{ref}$  reference pressure  
 $Re_\lambda$  Taylor Reynolds number  
 $r$  radial distance from the zero velocity location in the synthetic rotational and stagnation point flows

$S$  strain rate  
 $t_i$  instant of time for exposure  $i$   
 $\delta t$  time interval between exposures  
 $\bar{U}$  velocity  
 $U_e$  external free stream velocity  
 $\bar{U}_{13}$  velocity at  $t_2$  obtained by camera 1 based on images 1 and 3  
 $\bar{U}_{24}$  velocity at  $t_2 + \delta t$  obtained by camera 2 based on images 2 and 4  
 $\bar{U}_a$  averaged Lagrangian velocity between time  $t_2$  to  $t_2 + \delta t$   
 $W$  width of cavity  
 $\bar{x}_1$  location of particle group A at time  $t_1$   
 $\bar{x}_a$  location of particle group A at time  $t_2$   
 $\Delta$  residual of local cyclic integration of acceleration around a grid  
 $\Omega$  vorticity  
 $\nu$  kinematic viscosity  
 $\rho$  density of the fluid  
 $\omega$  rotation rate

## INTRODUCTION

Knowledge of the pressure distribution is a primary concern in many engineering applications. For a body moving in fluid, the pressure is responsible for both the lift and form drag acting on this body, the two key parameters in aircraft and marine vehicle designs. In turbulence research, the velocity-pressure-gradient tensor in the Reynolds stress transport equation, which is typically decomposed into the pressure diffusion and the pressure-strain tensors, is very important for understanding and modeling the turbulence [1-2]. However, due to the lack of the experimental capability, the velocity-pressure-gradient tensor has never been measured directly. It has only been inferred experimentally in simple geometries from a balance of the other terms in the turbulence kinetic energy transport equations [3-4].

Thus, except direct numerical simulation data, which is also limited to simple geometries and low Reynolds numbers, we have very little information on the velocity-pressure-gradient tensor.

Pressure is also of fundamental importance in understanding and modeling of cavitation. It is well established that cavitation inception occurs when small bubbles or nuclei in liquid grow explosively due to exposure to low pressure [5]. In the case of tip vortex cavitation, for example, Arndt [5] comments that direct measurements of pressure in the vortex core are rare. To date the only available techniques for pressure measurement away from boundaries are based on a Pitot-tube, such as five hole and seven hole probes. However, these probes are intrusive, not suitable for dynamic measurement due to a limited frequency response, and can only perform point measurements. This lack of adequate capability to determine the spatial pressure distribution, and the need of experimental data for both cavitation and turbulence research provide the motivation for the present effort. In this paper we introduce a system that is capable of measuring the instantaneous pressure distribution in a non-intrusive manner based on PIV technology. This system utilizes four-exposure PIV to measure the distribution of material acceleration, and then integrating it to obtain the pressure. This approach provides the instantaneous pressure, acceleration and velocity distributions simultaneously.

The material or Lagrangian acceleration has been studied both numerically and experimentally before. The objectives of most of previous works have been either to provide data for Lagrangian stochastic turbulence models [6-11], or to develop techniques for acceleration measurements [12-15]. Voth *et al* [9] used a large square photodiode to record individual particle tracks, and then calculated the acceleration of these particles in a turbulent flow between counter-rotating disks  $900 < \text{Re}_\lambda < 2000$ . La Porta *et al* [10] conducted acceleration measurements using a silicon strip detector to track individual particle trajectories in the same turbulent flow for  $\text{Re}_\lambda$  up to 63,000. Ott and Mann [11] used four synchronized CCD cameras to track the trajectories of seed particle pairs and investigated their diffusion characteristics in a turbulent flow generated by two oscillating grids. Jakobsen *et al* [12] utilized a specially designed four-CCD camera system to obtain the acceleration field near the wall of a surface wave flume based on particle image velocimetry (PIV) technology. They validated their acceleration measurement by integrating the averaged acceleration, and then comparing it to the mean pressure difference between two wall pressure taps. Dong *et al* [13] obtained two-dimensional Eulerian acceleration distributions using one CCD camera by combining cross-correlations and autocorrelations on two successive, doubly exposed frames to obtain two instantaneous velocity fields, which are used for computing the acceleration. Cross-correlations between the frames were used to resolve the directional ambiguity associated with the double exposures in each frame. Christensen and Adrian [14-15] measured the instantaneous Eulerian acceleration field of a boundary layer flow by using two CCD cameras with cross-polarized laser beams as light sources. They also calculated the so-called velocity bulk-convective-derivative field, and concluded that the dominant vortical structures remained almost frozen in time.

Sridhar and Katz [16] used triple exposure images to simultaneously measure the velocity and material acceleration of microscopic bubbles and the fluid surrounding them.

In this paper we extend the previous efforts, first by measuring the instantaneous distribution of material acceleration, and then by integrating it to measure the pressure distribution. The principles of the proposed technique are introduced in the next section, followed by calibrations using synthetic (artificially generated) flow fields. Then, the technique is implemented for measuring the instantaneous pressure distribution in a shear layer developing above a cavity.

## PRINCIPLE

Based on the Navier-Stokes equation, the pressure gradient can be expressed as

$$\nabla p = -\rho \left( \frac{D\bar{U}}{Dt} - \nu \nabla^2 \bar{U} \right) \quad (1)$$

Thus, if both of the material acceleration,  $D\bar{U}/Dt$ , and the viscous terms  $-\nu \nabla^2 \bar{U}$  can be measured directly, the pressure  $p$  can be integrated using equation 1. In a high Reynolds number flow field away from a wall, where there are no extremely high velocity gradients, the material acceleration is dominant and the viscous term is negligible. For example, Liu [17] and Thomas [18] found that the Reynolds-averaged viscous term in a turbulent near-wake experiment is  $10^{-5}$  times smaller than the peak value of the streamwise acceleration term. Neglecting the viscous term (requires verification), one has to measure the material acceleration and integrate it to determine the pressure, as aforementioned.

The present material acceleration measurement technique is based on its definition, while considering the inherent properties of PIV. A natural experimental approach would be to track the trajectory of a fluid particle, measure the time history of the velocity along this trajectory, and derive it to obtain the Lagrangian acceleration. Particle tracking methods have relied on this approach [9-11]. However, particle tracking can only provide data for a limited number of tracers, whereas the spatial integration to determine the pressure requires an instantaneous distribution over the entire region of interest. Fortunately, PIV measures the instantaneous velocity field and intrinsically, as pointed out by Jakobsen *et al* [12], the data is based the local velocity in the Lagrangian sense (displacement of particles). To measure the material acceleration, one has to compare the velocity of the same group of particles at two different times. The principles of the present approach are illustrated in Figure 1. We use a four-exposure PIV system with two ‘‘cross-correlation’’ cameras, which will be described in details later in this paper, to record four exposures of the particle traces within the sample area. The timing of the laser sheet pulses are denoted as  $t_1$ ,  $t_2$ ,  $t_3$  and  $t_4$ , and there is an equal time interval,  $\delta t$ , between them. Each image is recorded on a separate frame. Camera 1 records images 1 and 3, and the data are used to determine the first velocity distribution,  $\bar{U}_{13}$ . Camera 2 records images 2 and 4, which are used for calculating the second velocity map,  $\bar{U}_{24}$ .

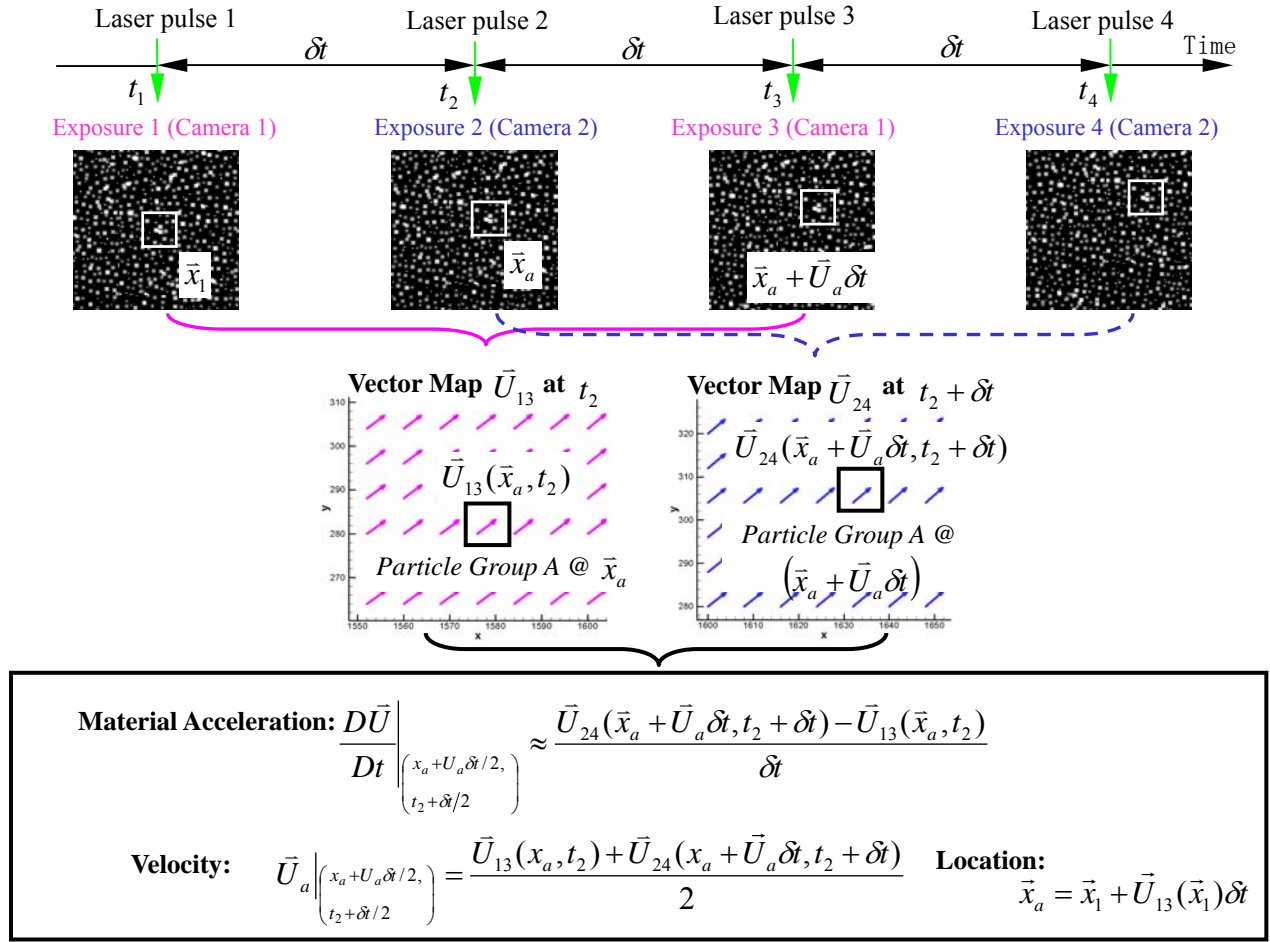


Figure 1. Schematic illustration of the material acceleration measurement technique.

Since intrinsically, cross-correlation PIV analysis tracks the displacement of the same group of seed particles between exposures, the local velocity determined by exposures 1 and 3 can be used to estimate the location of the same particle group during exposure 2. Similarly, the local velocity determined by exposures 2 and 4 can be used to estimate the location of the same particle group during exposure 3. Thus, a particle group located at  $\bar{x}_a$  when  $t = t_2$  has a velocity  $\bar{U}_{13}(\bar{x}_a)$ . At  $t_2 + \delta t$  (i.e. at  $t_3$ ), the same particle group is located at  $\bar{x}_a + \bar{U}_a \delta t$ , where

$$\bar{U}_a(\bar{x}_a + \bar{U}_a \delta t / 2, t_2 + \delta t / 2) = \frac{1}{2}(\bar{U}_{13}(\bar{x}_a, t_2) + \bar{U}_{24}(\bar{x}_a + \bar{U}_a \delta t, t_2 + \delta t)) \quad (2)$$

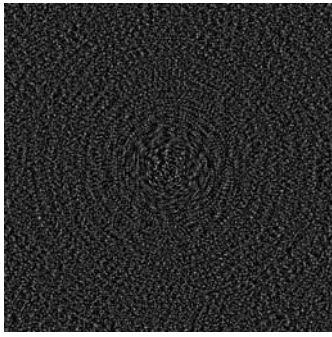
is the averaged Lagrangian velocity between  $t_2$  and  $t_2 + \delta t$ . This implicit expression requires iterations during data analysis. As a first approximation we typically choose  $\bar{U}_a^1 \approx \frac{1}{2}(\bar{U}_{13}(\bar{x}_a, t_2) + \bar{U}_{24}(\bar{x}_a, t_3))$  and then iterate to determine the correct value. Typically, about two iterations are sufficient to obtain a value that is less than the PIV uncertainty level from the asymptotic value. The material acceleration at  $\bar{x}_a + \bar{U}_a \delta t / 2$  and  $t = t_2 + \delta t / 2$ , determined by tracking a group of seed particles can then be estimated as:

$$\frac{D\bar{U}}{Dt} \Big|_{\substack{\bar{x}_a + \bar{U}_a \delta t / 2 \\ t_2 + \delta t / 2}} \approx \frac{\bar{U}_{24}(\bar{x}_a + \bar{U}_a \delta t, t_2 + \delta t) - \bar{U}_{13}(\bar{x}_a, t_2)}{\delta t} \quad (3)$$

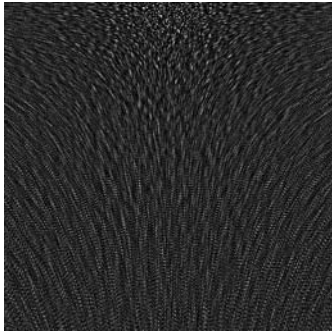
The (time) averaged Eulerian velocity distribution at the same time can be calculated by averaging the two vector maps, i.e.

$$\bar{U}(\bar{x}, t_2 + \delta t / 2) \approx \frac{1}{2}(\bar{U}_{1-3}(\bar{x}, t_2) + \bar{U}_{2-4}(\bar{x}, t_3)) \quad (4)$$

Integrating the material acceleration from a reference point with known pressure provides the pressure distribution  $p(\bar{x}, t_2 + \delta t / 2)$ , as long as the viscous terms are small. In 2-D PIV the measurements provides only two components of the velocity and material acceleration. However, the procedure described here assumes that the particles remain within the laser sheet as the four exposures are recorded. The purpose of calculating the first velocity field using exposures one and three ( $\bar{U}_{13}$ ) and the second field using exposures two and four ( $\bar{U}_{24}$ ) is to improve the chances that we indeed follow the same group of particles. In the following section we implement this procedure to calculate the pressure distribution in synthetic flow fields, and compare the computed and previously known pressure distributions.



(a)



(b)

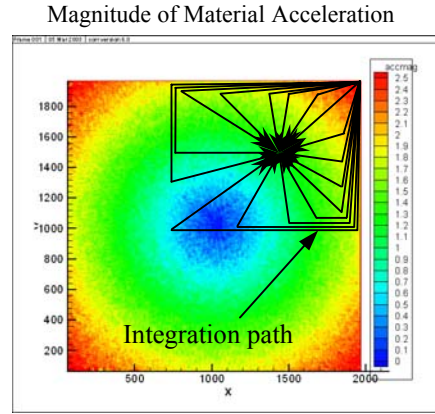
Figure 2. Synthetic images for (a) pure rotational flow and (b) stagnation point flow

Note that if 3-D data is available, e.g. from holographic PIV data, the acceleration can also be calculated in using an Eulerian approach. In this case one can calculate the local unsteady and convective terms of the acceleration at the same location.

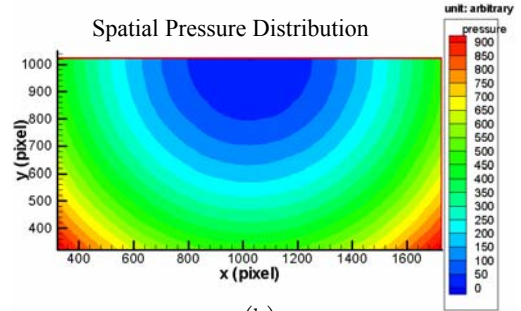
### SYNTHETIC FLOW RESULTS

To validate the principles of the pressure measurement technique, we use synthetic images of solid-body rotation and stagnation point flows. The simulated seed particles are distributed homogeneously in a 2048×2048 pixels image using a random number generator available in Matlab. The particle concentration is set to maintain an average of 25 particles per interrogation window of 32×32 pixels. The particle size has a Gaussian distribution, with a mean diameter of 2.4 pixels and a standard deviation of 0.8 pixels. The intensity is also Gaussian distributed, with a peak grayscale of 240. Based on the first synthetic image, the subsequent three planes are generated by displacing the particles according to the local theoretical velocity, using the analytical expressions for the velocity fields.

The selected rotation rate of the solid-body-rotation flow is  $\omega=0.0625/\text{sec}$ , and the constant strain rate for the stagnation point flow is  $S = 0.025/\text{sec}$ . The time interval between exposures is  $\delta t = 0.5 \text{ sec}$ . The resulting particle trajectories, visualized by overlapping the images are presented in Figure 2. For each set of four images we calculate two velocity fields,  $\vec{U}_{13}$  and  $\vec{U}_{24}$  using in-house developed PIV software described in Roth *et al* [19-20]. Using these velocity distributions, we calculate  $\vec{U}_a$ , and

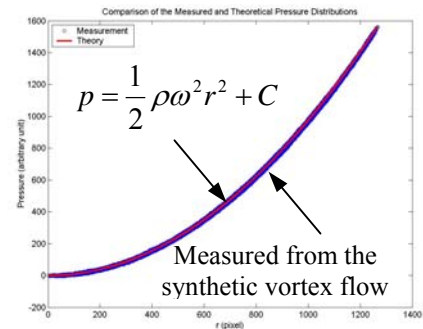


(a)

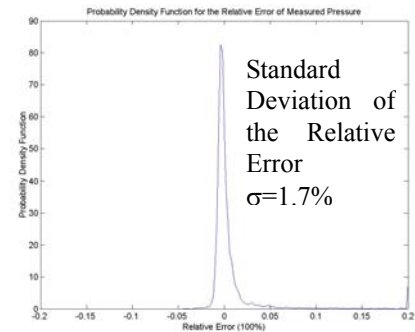


(b)

Figure 3. (a) Magnitude of the material acceleration and (b) spatial pressure distribution integrated from the material acceleration for the synthetic rotational flow.



(a)



(b)

Figure 4. (a) Radial pressure distribution and (b) probability density function of the relative error of pressure for the synthetic rotational flow.

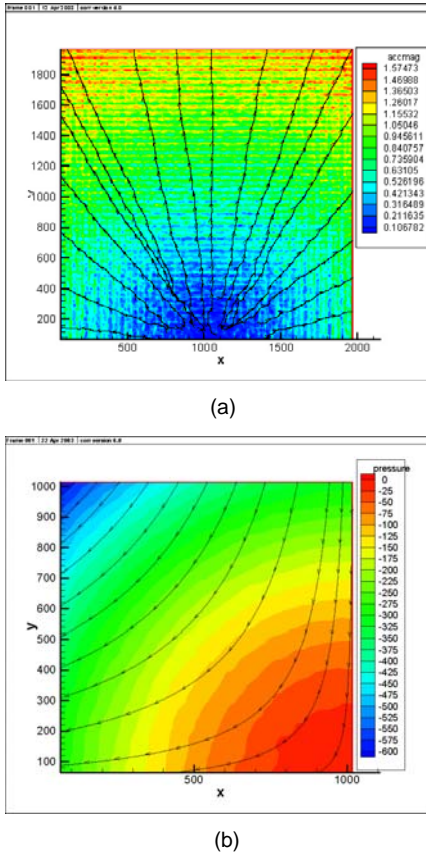


Figure 5. (a) Magnitude and streamlines of the material acceleration; (b) spatial pressure distribution integrated from the material acceleration and velocity streamlines for the synthetic stagnation flow.

subsequently the instantaneous material acceleration following the procedures described in the previous section.

Figure 3(a) shows the material acceleration magnitude iso-contour for the solid-body rotation. The irregularities are caused by errors that can be traced to the inherent uncertainty of the PIV analysis, and the truncation error of the finite difference scheme. These errors contaminate the calculated pressure and their effects must be minimized. Since the result of integration of pressure gradients must be independent of the integration path, to minimize the effect of the acceleration error, we implement an averaged, shortest path, omni-directional integration method, as illustrated in Figure 3(a). The resulting pressure iso-contours are illustrated in Figure 3(b). Unlike the acceleration, the irregularities disappear in the pressure distribution contours due to the omni-directional integration that acts as a low-pass filter. The measured radial pressure distribution is compared to the theoretical values in Figure 4(a). The degree of agreement is self-evident. The probability density function of the relative error of the pressure measurement, presented in Figure 4(b), has a standard deviation of 1.7%.

Figures 5(a) and (b) show the material acceleration and pressure, respectively, for the synthetic stagnation point flow. A comparison of the measured and the theoretical radial pressure distributions, along with the probability density function of the relative error is presented in Fig. 6. Here, the standard deviation of the relative error is 2.3%, slightly higher than that of the

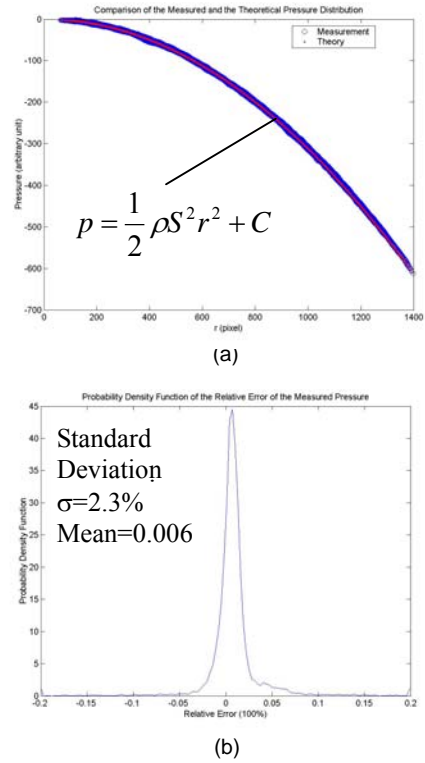


Figure 6. (a) Radial pressure distribution and (b) probability density function of the relative error of pressure for the synthetic stagnation flow.

rotational flow. The primary contributors to the increase in standard deviation are the coupled effect of the inherent “peak-locking” error of PIV analysis [20], and the 2.5 times lower dynamic range (lower typical displacement between exposures) of the present stagnation point flow [21]. Peak locking refers to a bias error at the sub-pixel level, which is associated with sub-pixel curve fitting to the discrete PIV correlation peaks. The peak locking causes the mesh-like distribution of acceleration since it introduces the same sub-pixel error on all the velocity components with the same sub-pixel velocity component. As the dynamic range increases, the relative significance of the peak locking effect diminishes. However, clearly in both synthetic examples the pressure distribution can be computed by integrating the material acceleration.

## EXPERIMENTAL SETUP

The pressure measurement technique is applied to a cavity shear flow in the small water tunnel, described in Gopalan and Katz [22]. The overall setup is described in Figure 7, and the test model is sketched in Figure 8. The 38.1mm long, 50.8mm wide and 30.0mm deep 2-D cavity is installed in the 50.8x63.5 mm test section. As shown, the test model has a contraction ramp leading to the cavity, and a diffusing ramp downstream of the cavity. A 13mm long region with tripping grooves having a notch depth of 0.46mm and opening of 1.00mm is machined at the beginning of the contraction ramp in order to trip the boundary layer. Figure 8 also shows the locations of three pressure transducers, which are needed for calibration. Custom polymer coated, Endevco 8510B-5, miniature, piezoresistive

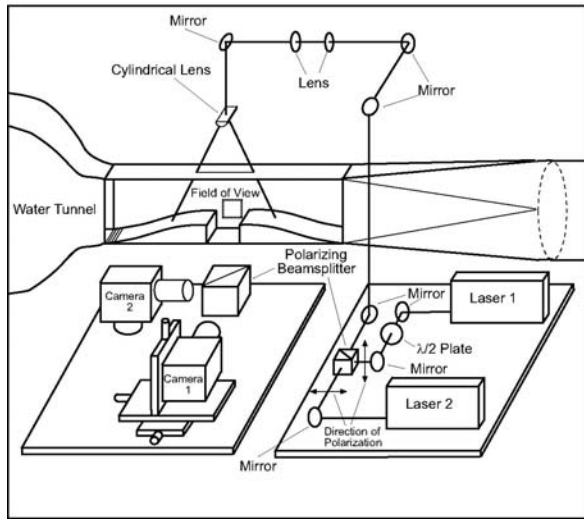


Figure 7. Optical set-up.

pressure transducers are currently being used. Earlier attempts to use miniature piezoelectric transducers (PCB 105B02) were abandoned due to response of the transducer to direct illumination by the laser.

The experimental setup is sketched in Figure 7. To record the four exposures we use two 2K×2K “cross-correlation” digital cameras with interline image transfer (Kodak ES4.0). Images 1 and 3 are recorded by camera 1 and images 2 and 4 are recorded by camera 2. The light sources are two dual-head Nd:Yag lasers, with flashes 1 and 3 generated by laser No. 1, and flashes 2 and 4 generated by laser No. 2. A half-wave plate is used for rotating the polarization of laser No. 1 before mixing the beams and expanding them to sheets. Consequently, the polarization angle of the light in pulses 1 and 3 is perpendicular to that of pulses 2 and 4. As discussed in Christensen and Adrian [15], most of the light reflected from tracer particles (hollow, 8-12 $\mu\text{m}$ , glass spheres with specific gravity of 1.05-1.15) located within the laser sheet maintains its polarization angle. Thus, by placing a polarizing beam splitter (cube) in front of the cameras, we can separate images 1 and 3 from images 2 and 4, and direct them on their respective cameras. The interline transfer feature of the cameras enables recording of each image on a separate frame.

### CAMERA ALIGNMENT AND CALIBRATION

It is essential to match the fields of view and magnification of the two cameras, requiring an elaborate alignment and calibration process. As a result, camera 1 is installed on a three-axis translation stage, while camera 2 is installed on a tilt and rotation stage (see Figure 7). A target with grid (Edmund Industrial Optics, model NT46-250), illuminated using incandescent light source, is placed in the test section. The plane of the target is aligned with the laser sheet to the best of our ability, considering that the sheet has a finite depth. The images of this target, as recorded by the two cameras, are compared to each other, and the differences between them are minimized by iteratively adjusting the focus of the lens and the settings of mounting stages.

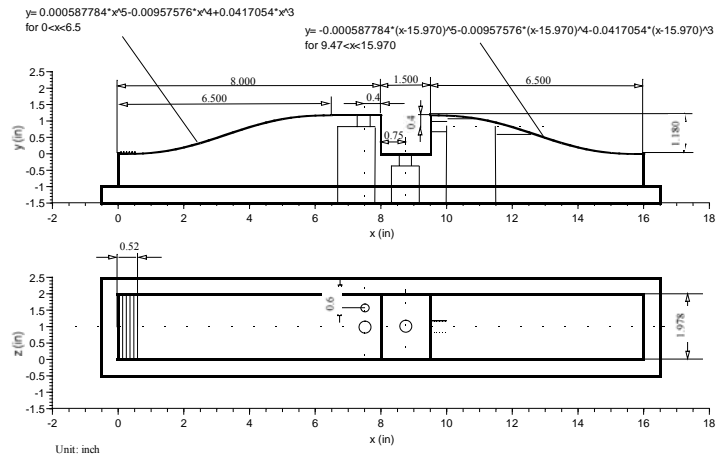


Figure 8. Experimental body for cavity shear flow.

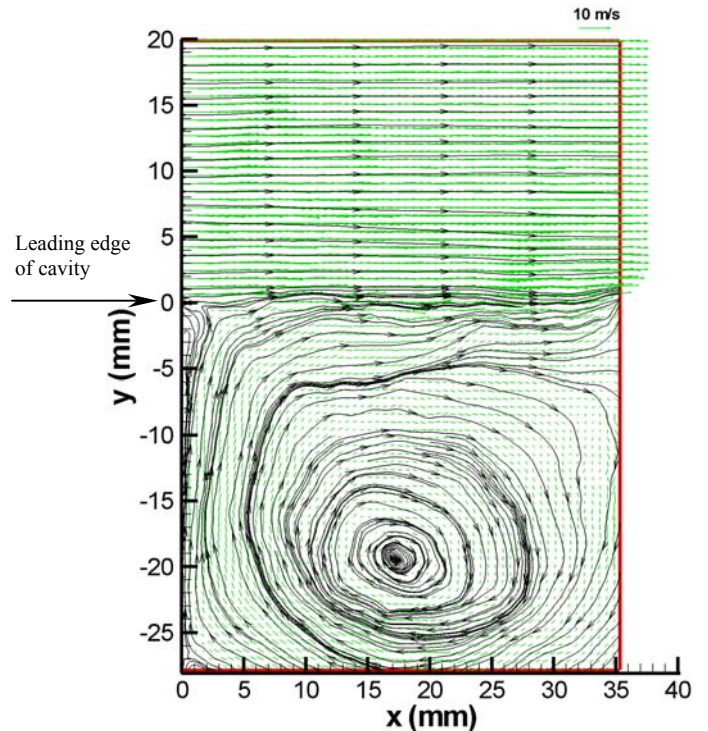


Figure 9. Instantaneous streamlines of the cavity shear flow at  $U_e = 10\text{m/s}$  and  $Re = 335,000$ .

Due to limitations of the mechanical alignment mechanism, no matter how much care is taken, it is virtually impossible to perfectly coincide the laser sheet with that of the target. For the 25.4×25.4mm field of view, a 0.05mm misalignment of the light sheet with the target results in a 4 pixels displacement on the image plane, which further corresponds to an acceleration error of 40,000 $\text{m/s}^2$ , an unacceptable level. Furthermore, differences in orientation and location cause location dependent shifts, whereas unavoidable lens-induced distortions cause location dependent variations in magnification. To overcome this problem, subsequent to the mechanical adjustments, we also compare images recorded by the two cameras of a laser sheet densely seeded with particles. These images are acquired at the same time by triggering both lasers simultaneously, with no flow in the test facility. Using cross-correlation analysis, similar to

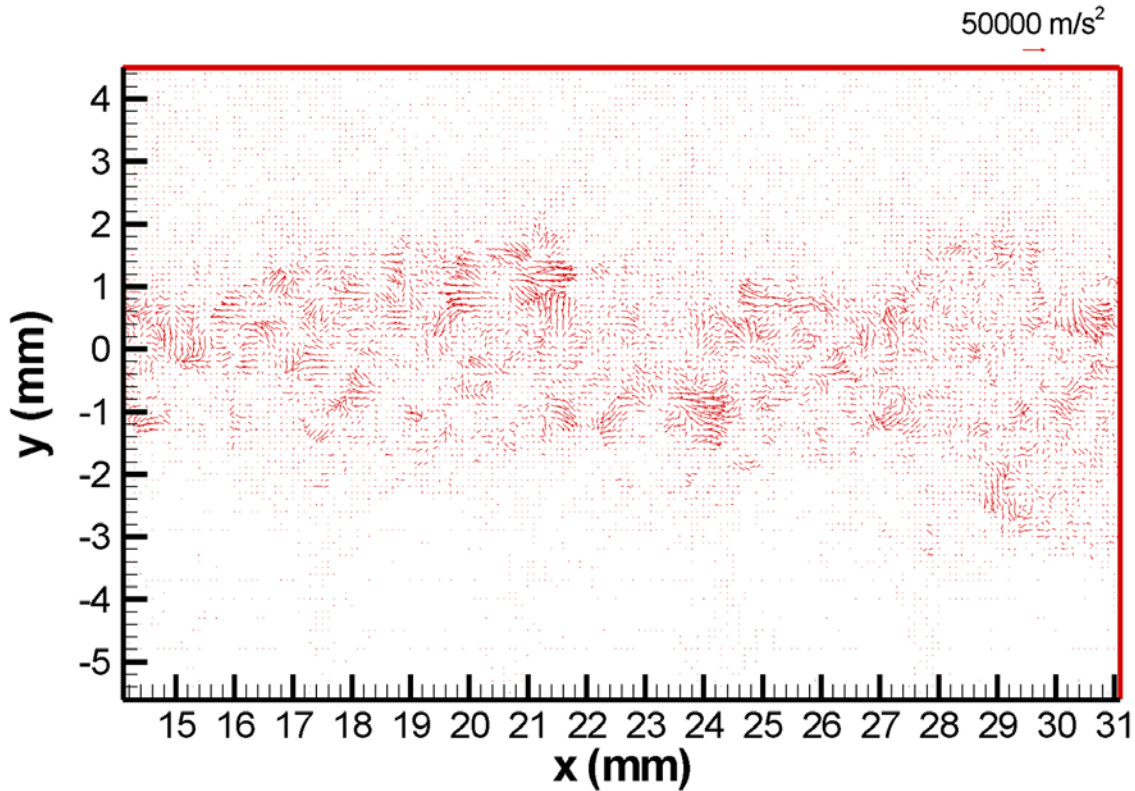


Figure 10. Sample material acceleration vector map within the cavity shear layer.

typical PIV procedures, we determine the spatial distribution of relative displacement between the two images. For the most part, these displacements are decomposed into relative translation, rotation and magnification difference between the two cameras. Using the resulting parameters, vector maps obtained by camera 2 are aligned with and adjusted to those obtained by camera 1. Following these corrections, the resulting vector maps only contain mostly errors due to lens-induced distortion of camera 1. However calibrations using the target show that this distortion is less than 0.003 pixel per pixel, much smaller than the typical accuracy of the PIV cross-correlation analysis (on the order of 0.1 pixel). Consequently, the effect of image distortion can be neglected.

### SAMPLE EXPERIMENTAL RESULTS

In the samples presented below, the origin of the coordinates is placed at the leading edge of the cavity and the x and y-axis are pointing downstream and upward, respectively. To illustrate the overall structure of the cavity flow, Figure 9 shows a sample instantaneous velocity distribution and streamlines of the cavity flow. Here the velocity above the cavity is 10m/s and the Reynolds number based on the cavity length is 335,000 based on the cavity width. Due to the unsteadiness of the shear layer, the impinging point of the shear layer on the downstream wall of the cavity varies significantly from one vector map to the next. In the example shown, the impingement point is located about 5mm below the corner. Several other secondary flow structures are also evident.

To maximize the spatial resolution of the acceleration measurements, we use progressive grid refinement, culminating

in  $32 \times 32$  pixels interrogation window with 75% overlap between windows. The corresponding length scales for a  $25.4 \times 25.4$ mm field of view are an interrogation window of  $0.4 \times 0.4$ mm, and vector spacing of 0.1 mm. For a  $50.8 \times 50.8$ mm field of view (both have been used), these dimensions are doubled. Following the procedures outlined earlier in this paper, we calculate the instantaneous distributions of material acceleration, and then integrate them to obtain the pressure distribution. Omni-directional integration is used to calculate the pressure in each point. To improve the accuracy of the integration, we circumvent regions with large acceleration errors. These regions are identified by the residual left after local cyclic integration of acceleration around a grid. The criterion for circumventing a point is the residual  $\Delta > 30000 \text{ m/s}^2$ .

A sample instantaneous vector map of the material acceleration, and a comparison of the resulting pressure field to the instantaneous vorticity distribution are presented in Figures 10 and 11, respectively. Here the velocity above the cavity is 5m/s and the Reynolds number based on the cavity length is 167,500. The local pressure at the upper left corner of the pressure map is selected as the reference pressure. As expected, the high pressure develops in regions of flow deceleration, and conversely, pressure minima develop in accelerating regions. The temporal contribution to the acceleration is of the same order of magnitude as that of the convective terms. Thus, the pressure minima are close to, but do not necessarily coincide with regions of high vorticity, considered to be likely sites of vortex centers. On the left side ( $x \approx 15$ mm) they coincide, but at  $x \approx 21$ mm, the instantaneous pressure minimum is located to the

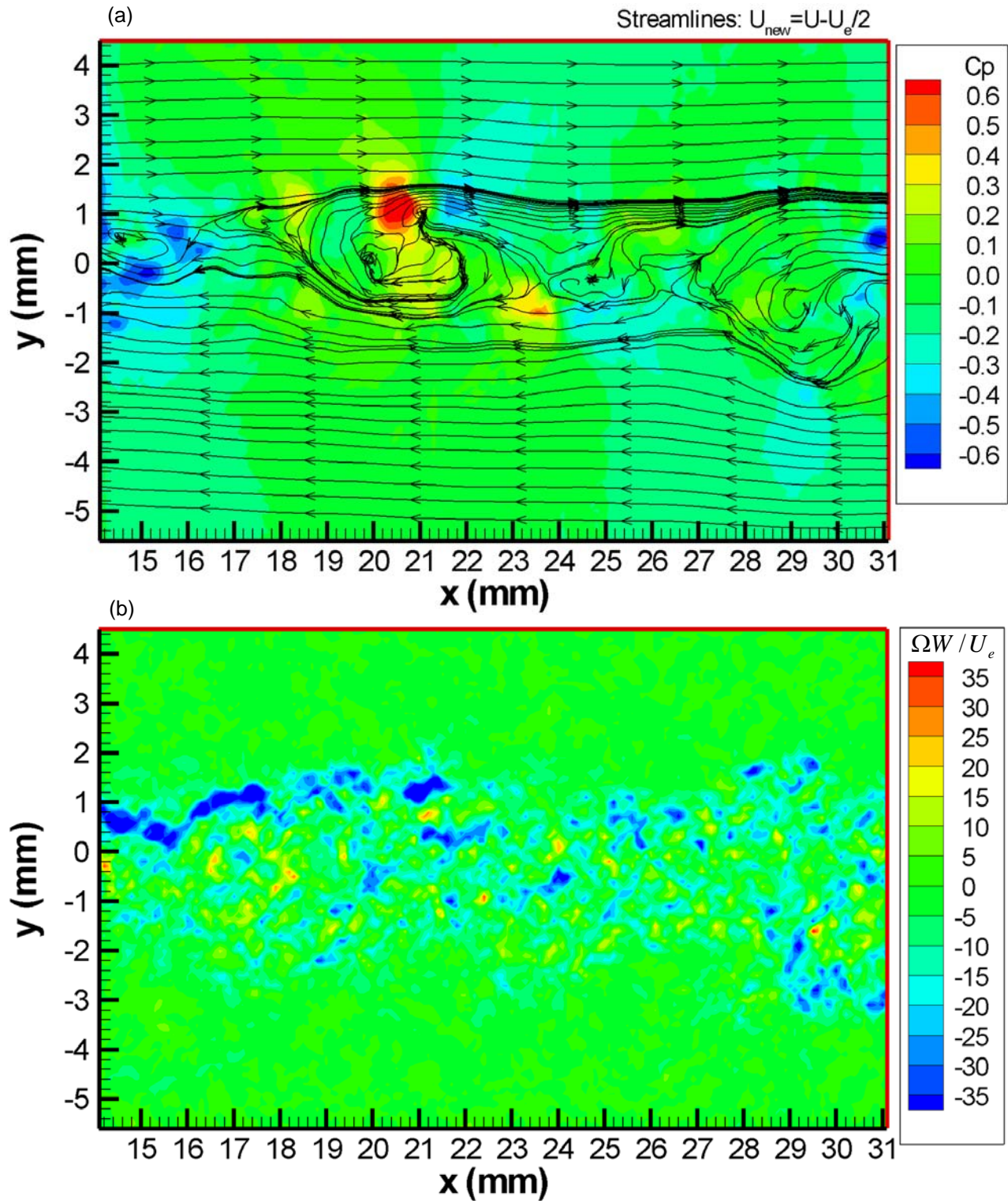


Figure 11. Comparison of (a) sample instantaneous pressure distribution and (b) the corresponding vorticity distribution in the shear layer.

right of the vorticity minimum. Note that the streamline structure overlaid on the pressure distribution is subjective, and varies significantly depending on which reference velocity is subtracted from each vector. Thus, it should not be used as an indicator for the presence of vortices.

### SUMMARY AND FUTURE PLANS

This paper introduces a method for non-intrusive, simultaneous measurements of the instantaneous velocity, material acceleration and pressure distributions. The principles of the procedure are validated using synthetic rotating and stagnation point flows. The standard deviation of the measured

instantaneous pressure from the theoretical value is less than 2.5%. The method has been used for measuring the measurement of a cavity shear flow. In the upcoming series of experiments, the data will be acquired simultaneously with wall pressure measurements. Both instantaneous readings and statistics will be compared. To obtain such pressure statistics, the data analysis procedures must be made efficient enough to handle thousands of instantaneous realizations.

We are also pursuing improvements to the data analysis procedures. For example, the present method calculates the acceleration from differences in velocity, and as a result, is affected by errors of both, which increases in regions with high velocity gradients. This process and the associated errors can be circumvented, relying on the cross correlation maps generated as part of the typical PIV analysis. Each correlation map has at least one peak corresponding to the mean displacement of the particles within the interrogation area. Cross correlations of the correlation maps of the 1-3 and 2-4 images generate peaks corresponding to the differences between them. The location of this peak, fitted at the sub-pixel levels, is a direct measure of the acceleration. If the locations of the interrogation windows corresponding to these maps are shifted by  $U_a \delta t$ , cross correlation of the correlation maps provides the material acceleration directly. Initial experimentation using this procedure looks very promising.

#### ACKNOWLEDGMENTS

This work is sponsored by the Office of Naval Research of the United States (Program Manager Dr. Ki-Han Kim). The authors would like to thank Yury Ronzhin for the mechanical design of the testing body and Stephen King for building the timing control device. Dr. Bo Tao's participation at the initial stage of this project and Dr. Shridhar Gopalan's valuable advice and assistance are also gratefully acknowledged.

#### REFERENCES

- [1] Pope, S.B., 2000, Turbulent flows, Cambridge Univ. press.
- [2] Girimaji, S.S., 2000, Pressure-strain correlation modelling of complex turbulent flows, *J. Fluid Mech.*, 422, 91-123.
- [3] Wygnanski, I. and Fiedler, H., 1969, Some measurements in the self-preserving jet, *J. Fluid Mech.*, 38, 577-612.
- [4] Gutmark, E and Wygnanski, I., 1976, The planar turbulent jet, *J. Fluid Mech.*, 73, 465-495.
- [5] Arndt, R.E.A., 2002, Cavitation in vortical flows, *Annu. Rev. Fluid Mech.* 34, 143-175.
- [6] Yeung, P.K., 2002, Lagrangian investigations of turbulence, *Annu. Rev. Fluid Mech.*, 34, 115-142.
- [7] Yeung, P.K., 2001, Lagrangian characteristics of turbulence and scalar transport in direct numerical simulations, *J. Fluid Mech.*, 427, 241-274.
- [8] Vedula, P. and Yeung, P.K., 1999, Similarity scaling of acceleration and pressure statistics in numerical simulations of isotropic turbulence, *Phys. Fluids*, 11, 1208-1220.
- [9] Voth, G.A., Satyanarayan, K. and Bodenschatz, E., Lagrangian acceleration measurements at large Reynolds numbers, *Phys. Fluids*, 10, 2268-2280.
- [10] La Porta, A., Voth, G.A., Crawford, A.M., Alexander, J. and Bodenschatz, E., 2001, Fluid particle accelerations in fully developed turbulence, *Nature*, 409, 1017-1019.
- [11] Ott, S. and Mann, J., 2000, An experimental investigation of the relative diffusion of particle pairs in three-dimensional turbulent flow, *J. Fluid Mech.*, 422, 207-223.
- [12] Jakobsen, M.L., Dewhirst, T.P. and Greated, C.A., 1997, Particle image velocimetry for predictions of acceleration fields and force within fluid flows, *Meas. Sci. Technol.*, 8, 1502-1516.
- [13] Dong, P., Hsu, T-Y, Atsavapranee, P., Wei, T. (2001), Digital particle image accelerometry, *Exp. Fluids*, 30: 626-632.
- [14] Christensen, K.T. and Adrian, R.J., 2001, Measurement of instantaneous acceleration fields using particle-image velocimetry, 4<sup>th</sup> Int. Symp. on PIV, PIV01 Paper 1080.
- [15] Christensen, K.T. and Adrian, R.J., 2002, Measurement of instantaneous Eulerian acceleration fields by particle-image velocimetry: method and accuracy, *Experiments in Fluids*, 33, 759-769.
- [16] Sridhar, G. and Katz, J., 1995, Drag and lift forces on microscopic bubbles entrained by a vortex, *Phys. Fluids*, 7, 389-399.
- [17] Liu, X., 2001, A study of wake development and structure in constant pressure gradient, Ph.D. dissertation, University of Notre Dame.
- [18] Thomas, F.O. and Liu, X., 2003, An experimental investigation of symmetric and asymmetric turbulent wake development in pressure gradient, submitted to *Physics of Fluids*.
- [19] Roth, G.I., 1998, Developments in particle image velocimetry (PIV) and their application to the measurement of the flow structure and turbulence within a ship bow wave, Ph.D. dissertation, Johns Hopkins University.
- [20] Roth, G.I. and Katz, J., 2001, Five techniques for increasing the speed and accuracy of PIV interrogation, *Meas. Sci. Technol.*, 12, 238-245.
- [21] Adrian, R.J., 1997, Dynamic ranges of velocity and spatial resolution of particle image velocimetry, *Meas. Sci. Technol.*, 8, 1393-1398.
- [22] Gopalan, S. and Katz, J., 2000, Flow structure and modeling issues in the closure region of attached cavitation, *Phys. Fluids*, 12, 895-911.

#### DISCUSSIONS

(to be added).